

# A new push-pull sample design for microscale mode I fracture toughness measurements under uniaxial tension

J.J. Schwiedrzik<sup>1,\*</sup>, J. Ast<sup>1</sup>, L. Pethö<sup>1</sup>, X. Maeder<sup>1</sup>, J. Michler<sup>1</sup>

<sup>1</sup>Empa Swiss Federal Laboratory for Material Science and Technology, Laboratory of Mechanics of Materials and Nanostructures, Thun, Switzerland

## Abstract

A sample geometry is proposed for performing microscale tensile experiments based on a push-pull design. It allows measuring mode I fracture toughness under uniform far-field loading. Finite element simulations were performed to determine the geometry factor, which was nearly constant for Young's moduli spanning 2 orders of magnitude. It was further verified that mode I stress intensity factor  $K_I$  is nearly constant over the width of the tension rods and an order of magnitude higher than  $K_{II}$  and  $K_{III}$ . Notched samples with different  $a/w$  ratios were prepared in (100)-oriented Si by a combination of reactive ion etching and focused ion beam milling. The mode I fracture toughness  $K_{I,q}$  was constant with  $a/w$  and in average  $1.02 \pm 0.06 \text{ MPa}\sqrt{\text{m}}$  in good agreement with existing literature. The geometry was characterized and experimentally validated and may be used for fracture toughness measurements of all material classes. It is especially interesting when a uniaxial, homogeneous stress field is desired, if crack tip plasticity is important, or when positioning of the indenter is difficult.

**Keywords:** Micromechanics, fracture toughness, single edge notch tension, push-pull design, silicon

---

\*Corresponding author. Email: [jakob.schwiedrzik@empa.ch](mailto:jakob.schwiedrzik@empa.ch)

24 **Nomenclature:**

25

$a$	Crack length
$a_0$	Initial notch depth
$b$	Rod width
$C$	Sample compliance
$C_0$	Unnotched sample compliance
$c_1, c_2$	Distance of rod 1 and 2 from the sample center
$C_{11}, C_{12}, C_{44}$	Cubic elastic constants
$C_{\text{initial}}$	Measured initial sample compliance
$f$	Geometry factor
$F$	Total applied force
$P_c, P_{c2}$	Force in rod 1 and 2
$K_I, K_{II}, K_{III}$	Critical stress intensity factors
$r$	Distance from crack tip
$r_{\text{pl}}$	Plastic zone size
$w$	Rod thickness
$\sigma_f$	Fracture stress

26

27

## 1. Introduction

The miniaturization of microelectronic devices and the use of thin hard coatings have led to an increased demand for knowledge on the fracture behavior of microscopic structures<sup>1</sup>. At the same time, many biological materials like bone or wood<sup>2</sup> possess a hierarchical microstructure spanning from the nano- to the macroscopic scale leading to a combination of antagonistic properties like strength and toughness and a strong scale effect<sup>3,4</sup>. Therefore, over the last 30 years an increasing number of microscale experiments have been proposed and properties of diverse materials have been measured<sup>1,5-8</sup>.

The development of silicon (Si) microfabrication techniques in large scale clean room facilities has allowed fabricating and commercializing microelectromechanical (MEMS) devices<sup>9</sup>. These structures require a high reliability, which motivates the mechanical characterization of their base materials. Si fails in a brittle manner at room temperature, its strength is defined as the stress needed to propagate a crack through the entire sample<sup>9</sup>. It depends on the maximum internal flaw size<sup>10</sup> and can vary significantly even within one batch.

The field of fracture mechanics deals with the analysis and prediction of the propagation of cracks and subsequent failure of a material; the material's resistance to fracture is characterized by its toughness. For measuring fracture toughness on the macroscale, different standard specimen geometries are proposed by the ASTM standard E399<sup>11</sup>. Most commonly single-edge notched bend (SENB), single-edge notched tension (SENT), compact tension (CT) or disk-shaped compact tension (DCT) specimens are used with atomically sharp fatigue starter notches. Those pre-cracks are in most cases either straight-through notches or chevron notches<sup>11,12</sup>, which have the advantage of promoting early crack initiation. Depending on the toughness and flow strength of the material different fracture mechanical parameters are used for the analysis. For brittle materials with a strongly limited amount of crack tip plasticity the stress intensity factor concept is applied<sup>11,12</sup>. For metallic materials with a higher toughness and ductility the crack growth re-

sistance curve (R-curve), must be determined, from which the fracture toughness can be measured. Established concepts are the J-Integral and the Crack-Tip-Opening-Displacement techniques<sup>13</sup>.

On the microscale, specimen preparation and handling is complicated by their small size and therefore different alternative methods have been proposed over the years. Many micromechanical fracture toughness measurements rely on nanoindentation<sup>14</sup> using sharp tips leading to the formation of cracks at the edges of the indenter. Depending on the observed crack type, e.g. radial, median, half-penny, lateral or conical, and the indenter shape (Berkovich or cube corner), the fracture toughness may be related to the crack initiation load, the crack size, hardness and elastic constants of the material, as well as the indenter geometry<sup>13–15</sup>. The relative ease of sample preparation and experimentation is in this case balanced by the complex stress fields around the indent and their interaction with the emerging crack that complicate the analysis<sup>15</sup>.

Alternative methods exist based on micropillar splitting by a sharp indenter<sup>8</sup>, double cantilever splitting<sup>16</sup>, or notched microcantilever<sup>17–20</sup>, and clamped beam bending<sup>21</sup>. These methods have been widely used<sup>8,16,22–24</sup> and shown to deliver consistent results<sup>25</sup>. In all these methods, the indenter needs to be placed with a high level of accuracy in order to obtain repeatable and consistent results making the use of in situ testing devices inside scanning electron microscopes especially attractive. This is not always possible, especially when tests have to be performed in controlled humidity or under liquid immersion, which is the case for many biological materials<sup>26–28</sup>. Furthermore, the stress far field in the specimens is not homogeneously tensile causing possible interactions of the crack tip with local compressive stresses. This may lead to crack deflections influencing the crack resistance behavior due to deviations from pure I mode loading.

Therefore, an alternative microscale sample is proposed here based on a symmetric push-pull design. It features a homogeneous, uniaxial stress far field in the tension rods. It is similar to the standard Single Edge Notch Tensile (SENT) sample geometry, for which an analytical solution for the stress intensity factor exists<sup>12,29,30</sup> with a relatively low geometry factor. Also, the sample is displaced using a flat punch indenter which makes it easy and fast to perform experiments and leads to a high level of robustness with respect to imprecise indenter positioning. Therefore, it features complementary properties compared to the established methods for microscale fracture toughness measurements making it an attractive alternative.

## 2. Sample shape optimization and mechanical characterization

First, the specimen geometry was optimized in a manual iterative procedure to obtain a uniaxial stress field in the tensile rods. A FEM model of the specimen geometry was implemented in the commercial solver Abaqus (Dassault Systems, USA), see Fig. 1. Only half of the sample was modeled and symmetry boundary conditions were applied in the middle of the sample. The flat punch indenter was modeled by kinematic coupling of the top surface to a reference node, which followed a prescribed downward movement. Linear elastic material behavior was chosen with the stiffness tensor of single crystal Si with cubic symmetry ( $C_{11}=165.6$  GPa,  $C_{12}=63.9$  GPa,  $C_{44}=79.5$  GPa<sup>31,32</sup>). The model was meshed with quadratic hexahedral elements (C3D20) and mesh convergence was verified by comparison of sample compliance as a function of characteristic element size. The mesh was judged to be converged globally when doubling the number of elements did not lead to an increase in sample compliance of more than 2%. The sample shape was iteratively optimized with respect to the ratio of width to length of the tensile rods, the width of the supporting structures, as well as the radii at the junction of the rods, in order to maximize the homogeneity of the maximum principal stress field within the tension rod, minimize stress concentrations at the junctions, and allow for production of the sample with a FIB/SEM workstation. The final geometry as well as the maximum principal stress distribution determined by FEM is presented in Fig. 1.

Subsequently, notches were introduced by crack seams and the stress field near the notch was treated using contour integrals. A  $\frac{1}{\sqrt{r}}$  stress singularity was introduced at the crack tip by collapsing the neighboring quadratic hexahedral elements into wedges and positioning the mid nodes at a quarter of the element length from the collapsed side. This is a standard method routinely applied in simulations of problems governed by linear elastic fracture mechanics. Five contour integrals were evaluated to estimate the stress intensity factors and the results of contour two to five were used in the following analysis. Local mesh convergence near the notches was verified by confirming that the average stress intensity factors for in-

creasing local mesh density in the vicinity of the crack tip were not increasing by more than 2%. It was found that  $K_I$  was in average one order of magnitude larger than both  $K_{II}$  and  $K_{III}$  (Fig. 2) so that the proposed geometry may be regarded as governed by mode 1 loading. Also,  $K_I$  was within 5% of its average over 95% of the specimen width and may therefore be considered constant (Fig. 2).

The notch depth  $a$  was varied in steps of  $0.5\mu\text{m}$  between  $1\mu\text{m}$  and  $4\mu\text{m}$  and the geometry factor  $f(a/w)$  was determined using the following equation<sup>11</sup> where it is assumed that the load is equally distributed on the two rods due to sample symmetry:

$$f\left(\frac{a}{w}\right) = \frac{2K_I b \sqrt{w}}{F} \quad (1)$$

with the notch depth  $a$ , rod thickness  $w$ , rod width  $b$ , and the force  $F$  applied by the flat punch indenter. A second order polynomial was fitted to the data points obtained by FEM resulting in a geometry factor function  $f_{\mu\text{SENT}}(a/w)$  of

$$f_{\mu\text{SENT}}\left(\frac{a}{w}\right) = 2.485 \left(\frac{a}{w}\right)^2 + 2.721 \left(\frac{a}{w}\right) + 0.401 \quad (2)$$

$f_{\mu\text{SENT}}(a/w)$  depends on the geometry only and is valid also for other materials than Si. An illustration of the geometry factor for the Micro-SENT sample compared to the single etch notch tensile (SENT) standard geometry may be seen in Fig. 3. The geometry factor of the SENT sample is given by<sup>30</sup>:

$$f_{\text{SENT}}\left(\frac{a}{w}\right) = \frac{\sqrt{2 \tan\left(\frac{\pi a}{2w}\right)}}{\cos\left(\frac{\pi a}{2w}\right)} \cdot \left(0.752 + 2.02 \left(\frac{a}{w}\right) + 0.37 \cdot \left(1 - \sin\left(\frac{\pi a}{2w}\right)\right)^3\right) \quad (3)$$

An excellent agreement with differences  $<10\%$  is found for  $a/w < 0.3$ . For higher  $a/w$  ratios, the geometry factors diverge.

In order to probe the robustness of the geometry factor with respect to geometrical imperfections, a Finite Element simulation of a tapered sample with an initial notch depth of  $2.5\mu\text{m}$ , a notch ground width of  $1.5\mu\text{m}$ , and a taper of approximately  $2^\circ$ , was performed. Computation of the geometry factor showed a

deviation of only 1.7% when using the average width in the analysis. It could thus be shown that K<sub>I</sub> is not strongly influenced by taper and that the analysis is robust with respect to this type of error.

Also, the effect of misalignment between the flat punch indenter and the sample was analyzed. For this, the full sample in frictionless, hard contact with a rigid flat punch indenter was modeled and the average stress intensity factors calculated from contour integrals on each notch were compared to the ideal case. It was found that for an in-plane misalignment between indenter and sample surface of 0.5°, the stress intensity factor K<sub>I</sub> at the two notches changed by ±5%; for 1° of misalignment, the relative error increased to ±12%. When considering out-of-plane misalignment, the relative error was +7 for 0.5° and +17% for 1°, -9% for -0.5° and -19% for -1° (positive angles correspond to a forward tilt of the indenter). Therefore, care has to be taken to achieve a good alignment between the indenter and the sample prior to testing. This is, however, a common need in many micromechanical experiments like nanoindentation, micropillar compression, etc., and not specific to this particular geometry.

Finally, the sample compliance C was determined as a function of normalized crack length for 0 < a/w < 0.5 (Fig. 4). When normalized by the unnotched sample compliance C<sub>0</sub>, it was well described by a third order polynomial of the crack length ratio a/w:

$$\frac{C}{C_0} = 1.8248 \left(\frac{a}{w}\right)^3 - 0.0024 \left(\frac{a}{w}\right)^2 + 0.054 \left(\frac{a}{w}\right) + 1 \quad (4)$$

This information may be used in future work for following the crack length by overlaying the ramp displacement loading with a sinus of small amplitude and measuring the dynamic stiffness as a function of tip displacement<sup>13,33–35</sup>. In this case, first the unnotched stiffness has to be determined based on the known notch depth and measured initial compliance C<sub>initial</sub>:

$$C_0 = \frac{C_{initial}}{1.8248 \left(\frac{a_0}{w}\right)^3 - 0.0024 \left(\frac{a_0}{w}\right)^2 + 0.054 \left(\frac{a_0}{w}\right) + 1} \quad (5)$$

Then, the crack depth can be determined from the measured apparent stiffness by inversion of  $\frac{C}{C_0} \left(\frac{a}{w}\right)$ :

$$\frac{a}{w} = 0.0044 - 35.71583 \cdot X^{-\frac{1}{3}} + 0.00028 \cdot X^{\frac{1}{3}} \quad (6)$$

141 with

$$X = -1.308 \cdot 10^{10} + 1.301 \cdot 10^{10} \cdot \left(\frac{C}{C_0}\right) + 11405 \cdot \sqrt{1.301 \cdot 10^{12} - 2.602 \cdot 10^{12} \cdot \left(\frac{C}{C_0}\right) + 1.301 \cdot 10^{12} \cdot \left(\frac{C}{C_0}\right)^2} \quad (7)$$

142 The crack progression can thus be monitored quasi-continuously, which enables the application of tech-  
 143 niques from elastic-plastic fracture mechanics (EPFM), like the J-Integral or crack tip opening displace-  
 144 ment (CTOD), described in detail in ASTM E 1820<sup>13</sup>. In this study, linear elastic fracture mechanics was  
 145 applied for the analysis of the experimental validation data on Si.

146

### 147 **3. Experimental study**

148

149 For experimental validation, a 8 µm wide freestanding wall was structured from a (100)-oriented Si wafer  
 150 to reduce FIB time. The wafer surface was spin coated with a photoresist, which was structured by direct  
 151 laser writing. For transferring the pattern into the silicon substrate, an inductively coupled plasma etcher  
 152 was used. Silicon was structured by alternating etching and passivation steps by SF<sub>6</sub> and C<sub>4</sub>F<sub>8</sub>. The etching  
 153 process results in a few 100 nm wide scalloping of the silicon sidewalls, which was reduced to 20 nm by  
 154 oxidation and subsequent oxide removal in a buffered HF solution.

155 The Micro-SENT shape was cut from the freestanding walls using a Ga<sup>+</sup> FIB-SEM workstation (Tescan  
 156 Lyra, Czech Republic) from the side. The protocol consisted of a rough cut at 30 kV and 10 nA followed  
 157 by notch milling at a reduced beam voltage of 15 kV and current of 100 pA. The notches were cut from  
 158 the front of the sample in the middle of the gauge section to obtain a homogeneous far field loading of the  
 159 notched section and a homogeneously sharp and flat notch ground, which can best be produced in this di-  
 160 rection using FIB. While lower currents theoretically result in sharper notches, the milling time and there-



by drift are significantly increased. Therefore, the beam settings used for notch milling in this study were a compromise between minimizing drift and obtaining the sharpest theoretical notch root radius<sup>34,35</sup>. Care was taken that the notch was wider than the final specimen width of 2  $\mu\text{m}$  to ensure a flat notch ground. Notches were milled on both tension rods in order to preserve the symmetry of the sample. The final sample shape was achieved by a fine polishing step at 30 kV and 1 nA. Using this protocol, very flat notch grounds with minimal rounding at the tension rod surfaces were achieved. The sample was oriented so that the tensile rods and notches were aligned with the crystal's  $\langle 100 \rangle$  directions. The preparation protocol and the final sample shape are illustrated in Fig. 5. Using the equilibrium of moments, the force in each arm may be computed as

$$P_{c1} = \frac{F \cdot c2}{c1 + c2} \quad (8)$$

and

$$P_{c2} = F - P_{c1} \quad (9)$$

For perfect symmetry,  $P_{c1}=F/2$ . Ten samples were prepared with notch depths of approximately 2.5  $\mu\text{m}$  ( $a_0/w=0.32$ ) and 3.3  $\mu\text{m}$  ( $a_0/w=0.41$ ). The Micro-SENT samples were tested using an in situ indenter (Alemnis AG, Switzerland) equipped with a 10  $\mu\text{m}$  flat punch diamond tip (Synton-MDP, Switzerland) inside a SEM (Zeiss DSM 962, Germany) at a constant displacement rate of 25 nm/s; force and tip displacement were monitored at 200 Hz sampling rate. The force-displacement curves were highly consistent and are shown in Fig. 6. The measured fracture loads were  $7.3 \pm 0.48$  mN (mean  $\pm$  standard deviation) and  $5.22 \pm 0.38$  mN, respectively.

Post-test high resolution SEM imaging of the fracture surfaces on a FIB-SEM workstation (Tescan Lyra, Czech Republic) revealed a flat notch ground and reproducible fracture patterns both within and between groups (Fig. 7). It was evident from the images that the fracture plane was aligned with the initial notch and the crystal's  $\{100\}$  plane. The fracture pattern consisting of dense arrays of fine straight lines suggests faceting of the crack, which runs globally parallel to the  $\{100\}$  plane, into local cleavage along  $\{110\}$  planes in line with literature<sup>36-39</sup>. This may be rationalized as follows: While cleavage happens locally

along {110} planes, the highest tensile stresses act on the {100} crack plane causing the crack to facet into many short segments. The asymmetry of the fracture surfaces is most probably caused by small misalignment of the flat punch with the sample, which led to the crack advancing in the left tension rod first. The right rod was then loaded under a combination of bending and tension, which explains the curved crack fronts visible on the right in Fig. 7. Due to the extreme brittleness of Si at room temperature, this asymmetric failure took place in a very short time and was not evident in either the in situ SEM video or the force-displacement data. Based on the earlier sensitivity analysis, it can be stated that the error in fracture toughness induced by misalignment is likely <10%. Inspection of the fracture surfaces allowed to measure the original notch depth  $a_0$  ( $2.5 \pm 0.05 \mu\text{m}$  and  $3.3 \pm 0.03 \mu\text{m}$ ) and rod width  $b$  ( $1.75 \pm 0.02 \mu\text{m}$  and  $1.71 \pm 0.02 \mu\text{m}$ ) of the two groups. The rod width reported here was determined by averaging the width at the notch ground and at the sample back surface (Fig. 7), which differed due to a sample taper of approximately  $2^\circ$ . By averaging the rod width for the analysis,  $K_{I,c}$  may be determined at high precision even in the presence of taper as shown by our finite element analysis. From the known geometry and fracture loads,  $K_{I,q}$  was determined using

$$K_{I,c} = \frac{P_{c,max}}{b\sqrt{w}} f\left(\frac{a}{w}\right) \quad (10)$$

for each specimen. Conditional data, denominated by the subscript q, was calculated, as not all criteria according to ASTM standard E399<sup>11</sup> such as sample size and quality of the starter notch can be met for tests at the microscale.

Two specimens were excluded from further analysis: One sample broke asymmetrically during testing as evidenced by the in situ SEM observation, the other one showed an oblique fracture plane and inconsistent fracture surface with the rest of the group in the post-test HRSEM observation. The results of the remaining eight samples are illustrated in Fig. 8. The experimental median of  $K_{I,q}$  was  $1.06 \text{ MPa}\sqrt{\text{m}}$  for  $a/w=0.32$  ( $n=4$ ) and  $0.99 \text{ MPa}\sqrt{\text{m}}$  for  $a/w=0.41$  ( $n=4$ ). No statistically significant difference was found between the two datasets with a Mann-Whitney test ( $p=0.49$ ), therefore the measured fracture toughness may be re-

garded independent of the notch depth and the two groups may be combined together. The resulting average mode I fracture toughness  $K_{I,q}$  was found to be  $1.02 \pm 0.06 \text{ MPa}\sqrt{\text{m}}$  ( $n=8$ ).

#### 4. Discussion

A new sample geometry called Micro-SENT was proposed in this work. It allows performing experiments in uniaxial tension using a standard flat punch indenter using a symmetric push-pull geometry. This enables measuring mode I fracture toughness under uniform far-field loading. The sample geometry was first optimized by a manual iterative procedure by FEM modeling to maximize the uniaxiality and homogeneity of the stress field within the tension rod while maintaining a shape that may be readily produced by FIB. The presence of a uniaxial, homogeneous far field increases the chance of a straight crack path, which leads to a high consistency and repeatability of the obtained results. Also, the use of a symmetric design and a flat punch makes the Micro-SENT setup relatively insensitive to errors in positioning of the indenter with respect to the sample, which is a great advantage in situations where a high resolution positioning is not possible or where image quality is insufficient. When using a flat punch, however, care must be taken to align indenter and sample well in order to keep errors at a minimum. Alternatively, the sample can also be loaded using a spherical indenter, which would reduce the error from misalignment of indenter and sample.

In-depth mechanical analysis by FEM using contour integrals showed that for a notched sample,  $K_I$  is almost constant over the rod width and one order of magnitude larger than  $K_{II}$  and  $K_{III}$ . This means that a measurement of  $K_{I,q}$  is possible with a good accuracy, as it dominates the stress field at the crack tip. It was verified that the stress levels at the notch ground are an order of magnitude higher than in the rest of the sample. Therefore, local plasticity due to stress concentrations at the rounded corners is not expected to play an important role in fracture toughness measurements. The geometry factor was determined by FEM and compared to the SENT sample geometry, for which an analytical solution exists<sup>12,29,30</sup>. Very

good correspondence with differences  $<10\%$  was found for  $a/w$  ratios  $<0.3$ . Furthermore, it was verified that varying the Young's modulus over 2 orders of magnitudes from 3 GPa to 411 GPa results in changes of less than 2% in the geometry factor. The similarity of the stress field and geometry function to an existing standard sample geometry (SENT) suggests that the results obtained by the new geometry are consistent with current standard methods. Furthermore, the geometry factor lies between 0.8 and 2.4 for  $0.125 < a/w < 0.5$  compared to geometry factors of 4 to 11 for the same range when considering common cantilever geometries<sup>25</sup>. This means that potentially the measured maximum force for a given material and  $a/w$  ratio will be higher for the Micro-SENT sample, which is especially important when testing brittle materials that fail at low loads near the noise floor of the instrument. Also, it is potentially less sensitive to errors in determination of the sample dimensions and notch depth, which is advantageous given the small length scales involved and length measurement uncertainties when using an SEM. It was verified that the presence of taper does not affect the measured fracture toughness values if the average sample width is used in the analysis. Furthermore, the influence of misalignment was assessed highlighting the need for careful indenter-sample alignment. Finally, the normalized compliance was determined as a function of crack length for  $0 < a/w < 0.5$ . This may be used for monitoring crack length by continuous stiffness measurement or partial unloading cycles during the fracture experiment when conducting nonlinear fracture mechanics analysis using J-integrals in the future<sup>13,33–35</sup>.

As the production process needs access with the ion beam from two orthogonal directions, samples have to be prepared from thin lamellae or on a polished edge in bulk samples. Also, the Micro-SENT sample design is relatively large to accommodate the symmetric design, guarantee a high stiffness of the guiding components as well as a high aspect ratio of the tensile rods. This can lead to long production times of several hours when using a standard  $\text{Ga}^+$  FIB for both rough pre patterning and final sample shaping. However, if freestanding structures are prefabricated with sufficient accuracy from thin lamellae, by lithographic methods, laser ablation, or Plasma-FIB, the production time can be reduced to less than one hour per sample in Si. In principal, the sample may be prepared from any class of material as long as the following requirements are met: Due to the need to produce the sample using FIB, the material needs to re-

main stable under high vacuum conditions and under the influence of electron beams. Non-conductive materials may also be used if coated by a thin conductive layer.

For experimental validation of the new method, notched samples were prepared from a (100)-oriented Si wafer by a combination of reactive ion etching and FIB and tested inside a scanning electron microscope. The measured mode I critical stress intensity factor  $K_{I,q}$  was found to be constant as a function of  $a/w$  and in average  $1.02 \pm 0.06 \text{ MPa}\sqrt{\text{m}}$  ( $n=8$ ). Reliable fracture toughness values for cleavage of single crystal silicon along (110) and (111) planes at room temperature in the literature vary from 0.65 to  $1.0 \text{ MPa}\sqrt{\text{m}}$ <sup>9,40-48</sup>. Micromechanical fracture measurements using several different methods resulted in room temperature fracture toughness values between 0.8 and  $1.0 \text{ MPa}\sqrt{\text{m}}$ <sup>25,49</sup>. Our results are located at the upper end of the spectrum of reliable toughness measurements for silicon<sup>9</sup> and feature a relatively small experimental scatter, therefore they may be regarded as in line with the existing research. Fracture surfaces imaged post-test revealed highly consistent and repeatable fracture patterns and faceted crack paths aligned with the (100) plane for both notch lengths. While the samples tested in this work featured a taper of approximately  $2^\circ$  due to the FIB production process, it was verified by finite element analysis that this has no significant effect on the analysis when using the average rod width. Also, taper may be significantly reduced in future studies by over-tilting the sample during the final FIB polishing step. It is noteworthy that the experimental variability is rather low when using the Micro-SENT sample compared to what is reported in literature for other microscale fracture tests on Si with standard deviations in the range of 10-15%<sup>25,49</sup>. The small variability is most probably due to the repeatable crack paths, the robustness of the sample geometry with respect to small variations in indenter placement and geometrical imperfections, as well as the small geometry factor. The sample was thus validated for silicon and may be used for testing the mode I fracture toughness of all classes of materials in the future.

In order to analyze the sources of experimental variability in further detail, an error propagation analysis was conducted based on the assumption of random independent errors<sup>50</sup> for the variables  $c_1$ ,  $c_2$ ,  $F$ ,  $b$ ,  $a$ , and  $w$ . For the force  $F$ , an error  $\Delta F = 10 \mu\text{N}$  based on the load cell noise was estimated. For all measured geometric dimensions in the SEM by means of high resolution images a conservative error of 100 nm was as-

sumed. Based on SEM images, the angular misalignment was estimated to be approximately  $0.5^\circ$ . The uncertainty resulting from error propagation analysis was then calculated as  $0.07 \text{ MPa}\sqrt{\text{m}}$  for no misalignment and  $0.12 \text{ MPa}\sqrt{\text{m}}$  when up to  $0.5^\circ$  misalignment in both directions is taken into account. This results in a total maximum error estimate of 13% when considering all error sources (experimental scatter, force and length measurement errors, misalignment) as independent. If experiments are performed inside a SEM allowing to determine the contact point with high precision, the sample could alternatively be loaded by a spherical indenter with a radius of approximately  $5 \text{ }\mu\text{m}$ , which would further reduce the error introduced by misalignment of the indenter tip.

It is very important to note that several requirements from the ASTM standard E399<sup>11</sup> cannot be or are very difficult to fulfill at the microscale. First of all, placing a fatigue starter notch at a specific location is very difficult to achieve, especially in brittle materials. Therefore, FIB notches were prepared, which are, however, not atomically sharp and may therefore lead to an overestimation of the fracture toughness. However, the root radius of notches prepared by  $\text{Ga}^+$  FIB is usually in the order of few tens of  $\text{nm}$ <sup>34,51,52</sup> and the crack can still be considered as sharp if the root radius is considerably smaller than the notch depth<sup>53</sup>. This was the case here, as the notch depth was 2 orders of magnitude larger than the notch root radius. Specimen size requirements are even more crucial for materials showing crack tip plasticity. For the present study, the plastic zone size was estimated using

$$r_{pl} = \frac{1}{2\pi} \left( \frac{K_{I,q}}{\sigma_f} \right)^2 \quad (11)$$

with the plastic radius  $r_{pl}$ , the fracture toughness  $K_{I,q}$ , and the fracture stress  $\sigma_f$ . Using the experimentally measured fracture toughness of  $1.02 \text{ MPa}\sqrt{\text{m}}$  and a room temperature fracture stress of  $6 \text{ GPa}$ <sup>54</sup> from micropillar compression experiments, a plastic zone radius of approximately  $5 \text{ nm}$  is computed. Therefore, dimensions in the micron regime are sufficient and significantly larger than the plastic zone size. Also the requirement concerning the thickness to width ratio  $1 < w/b < 4$  is fulfilled in the experiments. Therefore, the microscale fracture toughness measurements described here achieved a high level of consistency even though not all requirements of ASTM standard E399<sup>11</sup> could be met. This is reflected also in the good cor-

308 response of the fracture toughness reported here ( $1.02 \text{ MPa}\sqrt{\text{m}}$ ) with the range of values regarded as  
309 reliable in the literature ( $0.65\text{-}1.0 \text{ MPa}\sqrt{\text{m}}$ )<sup>9</sup>.

310  
311 **5. Conclusion**

312  
313 The proposed symmetric push-pull sample geometry called Micro-SENT sample was thoroughly charac-  
314 terized by FEM and validated experimentally on Si. It may be used for testing microscale fracture tough-  
315 ness of all classes of materials in situations where a uniform stress far field is desirable, a high consistency  
316 of the measured critical stress intensity factor measurements is needed, or a precise positioning of indenter  
317 on the sample is difficult to achieve.

318  
319 **6. Acknowledgements**

320  
321 The authors would like to thank A. Böll, G. Bürki, and D. Frey of the Laboratory for Mechanics of Mate-  
322 rials and Nanostructures of Empa for their help with manufacturing, SEM, and instrumentation issues.

323  
324 **7. Conflict of Interest**

325  
326 The authors declare no conflict of interest.  
327

## 8. References

1. Srikar, V. & Spearing, S. (2003). A critical review of microscale mechanical testing methods used in the design of microelectromechanical systems. *Experimental mechanics* 43 (3), 238–247
2. Fratzl, P. & Weinkamer, R. (2007). Nature's hierarchical materials. *Progress in Materials Science* 52 (8), 1263–1334, doi:10.1016/j.pmatsci.2007.06.001
3. Ritchie, R. O., Buehler, M. J. & Hansma, P. (2009). Plasticity and toughness in bone. *Physics Today* 62 (6), doi:10.1063/1.3156332
4. Schwiedrzik, J. *et al.* (2014). In situ micropillar compression reveals superior strength and ductility but an absence of damage in lamellar bone. *Nature Materials* 13 (7), 740–747
5. Uchic, M. D. & Dimiduk, D. M. (2005). A methodology to investigate size scale effects in crystalline plasticity using uniaxial compression testing. *Materials Science and Engineering: A* 400, 268–278
6. Gerberich, W. *et al.* (2009). Scale effects for strength, ductility, and toughness in brittle materials. *Journal of Materials Research* 24 (03), 898–906
7. Greer, J. R. & De Hosson, J. T. M. (2011). Plasticity in small-sized metallic systems: Intrinsic versus extrinsic size effect. *Progress in Materials Science* 56 (6), 654–724
8. Sebastiani, M., Johanns, K., Herbert, E. G. & Pharr, G. M. (2015). Measurement of fracture toughness by nanoindentation methods: Recent advances and future challenges. *Current Opinion in Solid State and Materials Science* 19 (6), 324–333
9. DelRio, F. W., Cook, R. F. & Boyce, B. L. (2015). Fracture strength of micro- and nano-scale silicon components. *Applied Physics Reviews* 2 (2), 021303, doi:10.1063/1.4919540
10. Griffith, A. (1921). The phenomena of flow and rupture in solids. *Phil. Trans. A* 221
11. ASTM Standard E399-90 (ASTM International, West Conshohocken, PA: 1997). *Standard Test Method for Plane-Strain Fracture Toughness of Metallic Materials*.
12. Anderson, T. (CRC press, Boca Raton: 2005). *Fracture mechanics: fundamentals and applications*.
13. ASTM Standard E1820 (ASTM International, West Conshohocken, PA: 1999). *Standard Test Method for Measurement of Fracture Toughness*.
14. Oliver, W. C. & Pharr, G. M. (1992). An improved technique for determining hardness and elastic modulus using load and displacement sensing indentation experiments. *Journal of Materials Research* 7 (06), 1564–1583
15. Lee, J., Gao, Y., Johanns, K. & Pharr, G. (2012). Cohesive interface simulations of indentation cracking as a fracture toughness measurement method for brittle materials. *Acta Materialia* 60 (15), 5448–5467
16. Liu, S., Wheeler, J., Howie, P., Zeng, X., Michler, J. & Clegg, W. (2013). Measuring the fracture resistance of hard coatings. *Applied Physics Letters* 102 (17), 171907
17. Di Maio, D. & Roberts, S. (2005). Measuring fracture toughness of coatings using focused-ion-beam-machined microbeams. *Journal of materials research* 20 (02), 299–302
18. Matoy, K., Detzel, T., Müller, M., Motz, C. & Dehm, G. (2009). Interface fracture properties of thin films studied by using the micro-cantilever deflection technique. *Surface and Coatings Technology* 204 (6), 878–881
19. Wurster, S., Motz, C. & Pippan, R. (2012). Characterization of the fracture toughness of micro-sized tungsten single crystal notched specimens. *Philosophical Magazine* 92 (14), 1803–1825



20. Žagar, G., Pejchal, V., Mueller, M. G., Michelet, L. & Mortensen, A. (2016). Fracture toughness measurement in fused quartz using triangular chevron-notched micro-cantilevers. *Scripta Materialia* 112, 132–135
21. Jaya, B. N. & Jayaram, V. (2014). Crack stability in edge-notched clamped beam specimens: modeling and experiments. *International Journal of Fracture* 188 (2), 213–228
22. Armstrong, D., Haseeb, A., Roberts, S., Wilkinson, A. & Bade, K. (2012). Nanoindentation and micro-mechanical fracture toughness of electrodeposited nanocrystalline Ni–W alloy films. *Thin Solid Films* 520 (13), 4369–4372
23. Iqbal, F., Ast, J., Göken, M. & Durst, K. (2012). In situ micro-cantilever tests to study fracture properties of NiAl single crystals. *Acta Materialia* 60 (3), 1193–1200
24. Trembl, R. *et al.* (2016). Miniaturized fracture experiments to determine the toughness of individual films in a multilayer system. *Extreme Mechanics Letters* 8, 235–244
25. Jaya, B. N., Kirchlechner, C. & Dehm, G. (2015). Can microscale fracture tests provide reliable fracture toughness values? A case study in silicon. *Journal of Materials Research* 30 (05), 686–698
26. Rodriguez-Florez, N., Oyen, M. L. & Shefelbine, S. J. (2013). Insight into differences in nanoindentation properties of bone. *Journal of the Mechanical Behavior of Biomedical Materials* 18, 90–99
27. Mirzaali, M., Schwiedrzik, J. J., Thaiwichai, S., Zysset, P. K. & Wolfram, U. (2016). Mechanical properties of cortical bone and their relationships with age, gender, composition and microindentation properties in the elderly. *Bone* 93, 196–211
28. Bertinetti, L., Hangen, U. D., Eder, M., Leibner, P., Fratzl, P. & Zlotnikov, I. (2015). Characterizing moisture-dependent mechanical properties of organic materials: humidity-controlled static and dynamic nanoindentation of wood cell walls. *Philosophical Magazine* 95 (16–18), 1992–1998
29. Gross, B., Srawley, J. E. & Brown Jr, W. F. (DTIC Document: 1964). *Stress-intensity factors for a single-edge-notch tension specimen by boundary collocation of a stress function.*
30. Tada, H., Paris, P. C. & Irwin, G. R. (Paris Productions: 1985). *The Stress Analysis of Cracks Handbook.*
31. Mason, W. (van Nostrand, Princeton: 1958). *Physical Acoustics and the Properties of Solids.*
32. Hopcroft, M. A., Nix, W. D. & Kenny, T. W. (2010). What is the Young's Modulus of Silicon? *Journal of microelectromechanical systems* 19 (2), 229–238
33. Kupka, D. & Lilleodden, E. (2012). Mechanical testing of solid–solid interfaces at the microscale. *Experimental Mechanics* 52 (6), 649–658
34. Ast, J., Przybilla, T., Maier, V., Durst, K. & Göken, M. (2014). Microcantilever bending experiments in NiAl—Evaluation, size effects, and crack tip plasticity. *Journal of Materials Research* 29 (18), 2129–2140
35. Ast, J., Merle, B., Durst, K. & Göken, M. (2016). Fracture toughness evaluation of NiAl single crystals by microcantilevers—a new continuous J-integral method. *Journal of Materials Research* 31 (23), 3786–3794, doi:10.1557/jmr.2016.393
36. Kohlhoff, S., Gumbsch, P. & Fischmeister, H. F. (1991). Crack propagation in b.c.c. crystals studied with a combined finite-element and atomistic model. *Philosophical Magazine A* 64 (4), 851–878, doi:10.1080/01418619108213953
37. George, A. & Michot, G. (1993). Dislocation loops at crack tips: nucleation and growth—an experimental study in silicon. *Materials Science and Engineering: A* 164 (1–2), 118–134
38. Li, X. *et al.* (2005). Measurement for fracture toughness of single crystal silicon film with tensile test. *Sensors and Actuators A: Physical* 119 (1), 229–235, doi:http://dx.doi.org/10.1016/j.sna.2003.10.063
39. Kermode, J. R. *et al.* (2008). Low-speed fracture instabilities in a brittle crystal. *Nature* 455 (7217), 1224–1227, doi:10.1038/nature07297

40. Gilman, J. J. (1960). Direct Measurements of the Surface Energies of Crystals. *Journal of Applied Physics* 31 (12), 2208–2218, doi:10.1063/1.1735524
41. Jaccodine, R. J. (1963). Surface Energy of Germanium and Silicon. *Journal of The Electrochemical Society* 110 (6), 524, doi:10.1149/1.2425806
42. John, C. S. (1975). The brittle-to-ductile transition in pre-cleaved silicon single crystals. *Philosophical Magazine* 32 (6), 1193–1212, doi:10.1080/14786437508228099
43. Brede, M. & Haasen, P. (1988). The brittle-to-ductile transition in doped silicon as a model substance. *Acta Metallurgica* 36 (8), 2003–2018, doi:10.1016/0001-6160(88)90302-1
44. Chen, C. P. & Leipold, M. H. (1980). Fracture toughness of Silicon. *The American Ceramics Society Bulletin* 59 (4)
45. Bhaduri, S. B. & Wang, F. F. Y. (1986). Fracture surface energy determination in {1 1 0} planes in silicon by the double torsion method. *Journal of Materials Science* 21 (7), 2489–2492, doi:10.1007/BF01114295
46. Haerle, A. G., Cannon, W. R. & Denda, M. (1991). Direct Measurement of Crack Tip Stresses. *Journal of the American Ceramic Society* 74 (11), 2897–2901, doi:10.1111/j.1151-2916.1991.tb06860.x
47. Connally, J. A. & Brown, S. B. (1992). Slow Crack Growth in Single-Crystal Silicon. *Science* 256 (5063), 1537–1539, doi:10.1126/science.256.5063.1537
48. Connally, J. A. & Brown, S. B. (1993). Micromechanical fatigue testing. *Experimental Mechanics* 33 (2), 81–90, doi:10.1007/BF02322482
49. Jaya, B. N. *et al.* (2016). Microscale Fracture Behavior of Single Crystal Silicon Beams at Elevated Temperatures. *Nano Letters* 16 (12), 7597–7603
50. Taylor, J. R. (University Science Books, Sausalito: 1982). *An introduction to error analysis*.
51. Mueller, M. G., Pejchal, V., Žagar, G., Singh, A., Cantoni, M. & Mortensen, A. (2015). Fracture toughness testing of nanocrystalline alumina and fused quartz using chevron-notched microbeams. *Acta Materialia* 86, 385–395, doi:http://doi.org/10.1016/j.actamat.2014.12.016
52. Shorubalko, I., Pillatsch, L. & Utke, I. (2016). Direct-Write Milling and Deposition with Noble Gases. *Helium Ion Microscopy*, 355–393
53. Picard, D., Leguillon, D. & Putot, C. (2006). A method to estimate the influence of the notch-root radius on the fracture toughness measurement of ceramics. *Journal of the European Ceramic Society* 26 (8), 1421–1427
54. Korte, S., Barnard, J. S., Stearn, R. J. & Clegg, W. J. (2011). Deformation of silicon – Insights from micro-compression testing at 25–500 °C. *International Journal of Plasticity* 27 (11), 1853–1866, doi:http://doi.org/10.1016/j.ijplas.2011.05.009

**Fig. 1: Maximum principal stress distribution on the proposed unnotched sample shape. Left: Front view, only the left half of the specimen was modeled due to the symmetry of the sample geometry. Maximum principle stress is approximately constant in the middle quadrant of the gauge section, where the notch is prepared for fracture mechanics experiments. Right: Cut through the tension rod perpendicular to the sample front surface. Sample dimensions are given in  $\mu\text{m}$ .**

**Fig. 2: Stress intensity factor distribution over the rod width normalized by the average  $K_I$  for  $a/w=0.25$ .**

**Fig. 3: Geometry factor  $f(a/w)$  of the Micro-SENT sample determined by FEM simulations for  $0.125 < a/w < 0.5$  compared to the geometry factor of the SENT sample. An excellent agreement between the geometry factors with deviations  $< 10\%$  is found for  $a/w < 0.3$ .**

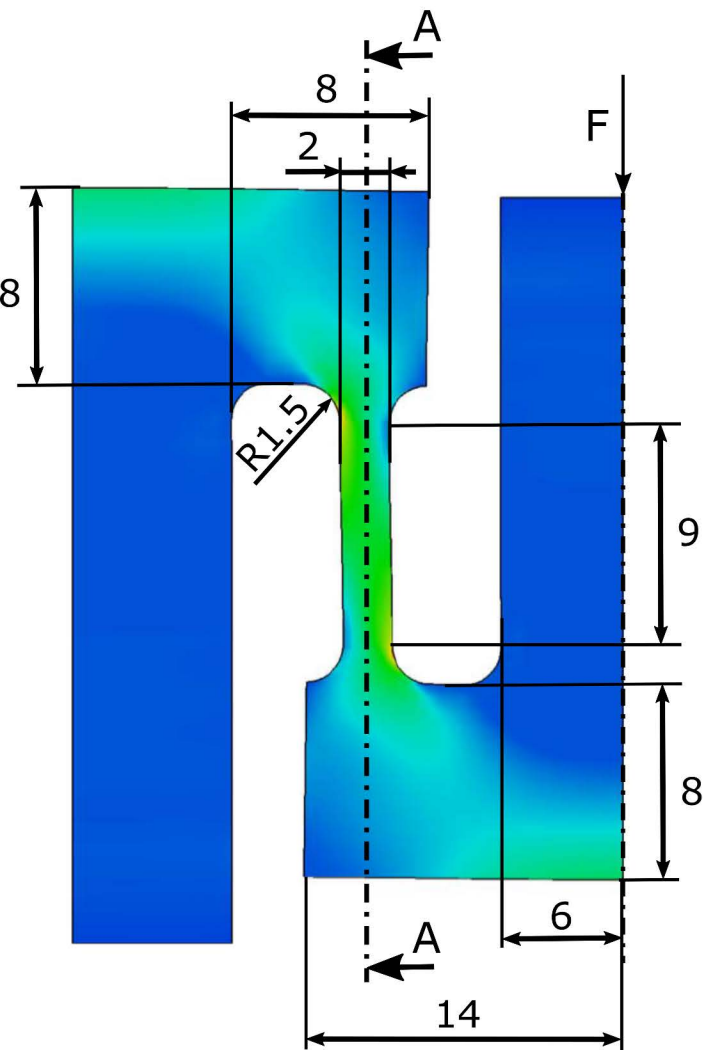
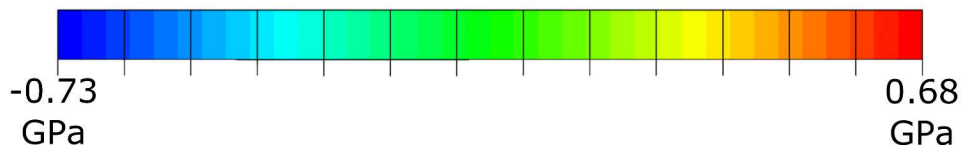
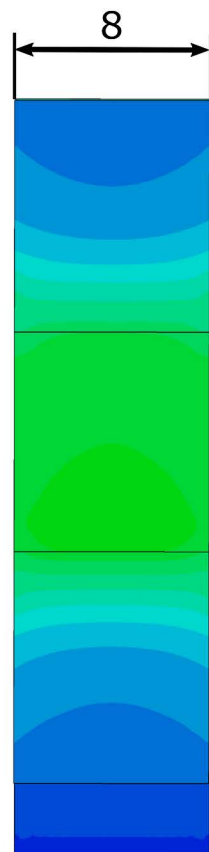
**Fig. 4: Micro -SENT sample compliance normalized by the unnotched sample  $C/C_0$  as a function of crack length ratio for  $0 < a/w < 0.5$ .**

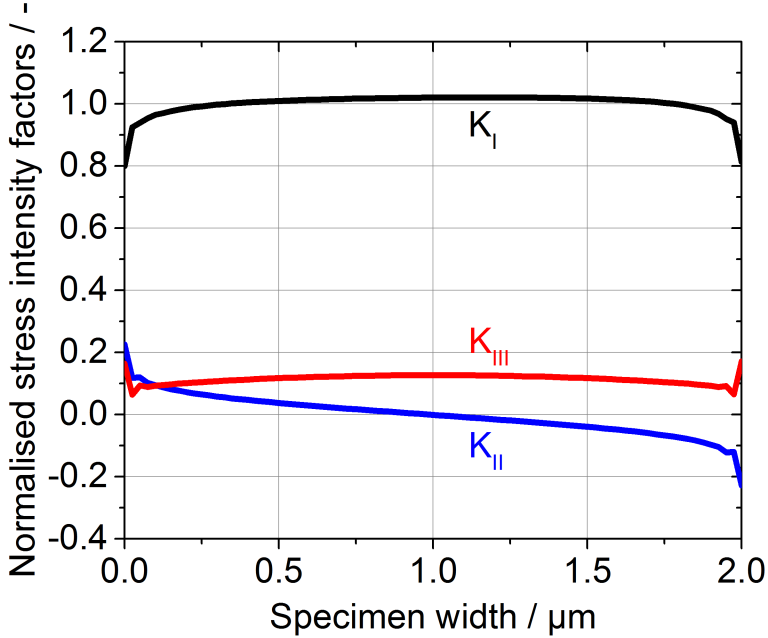
**Fig. 5: Sketch of the protocol for producing the Micro -SENT sample using a focused ion beam consisting of a) rough milling at 30kV and 10nA, b) notch cutting at 15kV and 100pA, and c) fine polishing at 30kV and 1nA. The final sample shape is illustrated for a Si sample for which the tensile rods and notches are aligned with the crystal's  $\langle 100 \rangle$  directions. Sample dimensions in the figure are given in  $\mu\text{m}$ .**

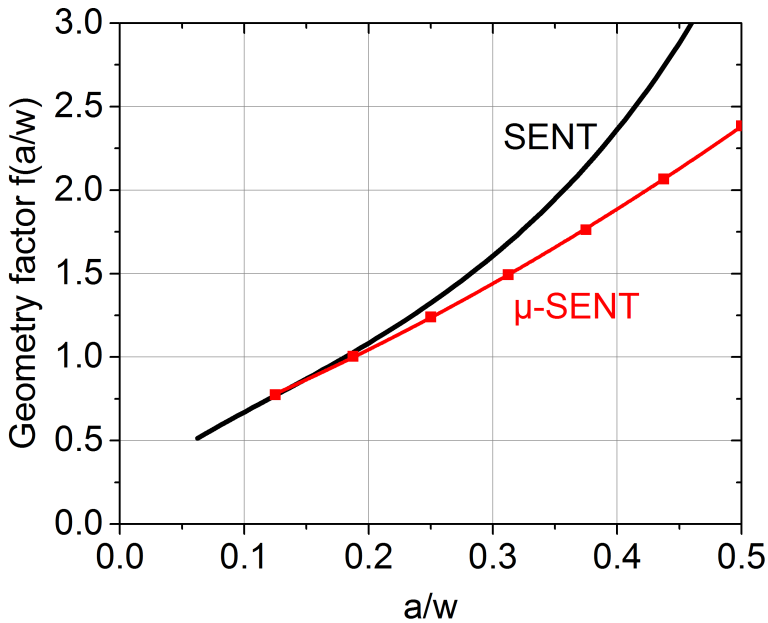
**Fig. 6: Force-displacement curves of the fracture toughness experiments on (001)-oriented silicon using the Micro-SENT geometry for  $a/w=0.32$  and  $a/w=0.41$ . Black crosses indicate fracture loads.**

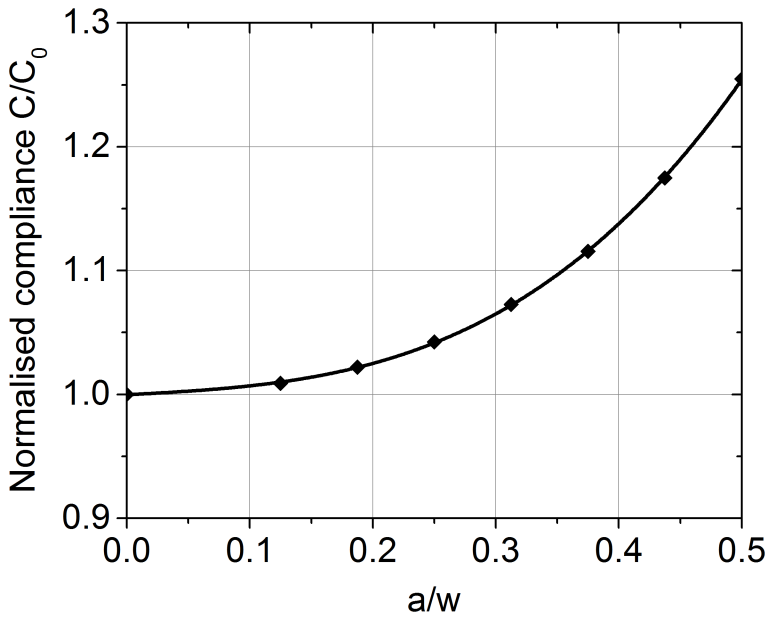
**Fig. 7: Fracture surfaces for  $a/w=0.32$  (a and b) and  $a/w=0.41$  (c and d) showing a flat notch ground and reproducible fracture patterns. Fracture occurred along  $\{110\}$  cleavage planes with a straight crack path. The asymmetric fracture pattern suggests that the left rod failed first and the right rod was then loaded by a combination of tension and bending. The scale bar represents  $1\text{ }\mu\text{m}$ .**

**Fig. 8: Fracture toughness  $K_{I,q}$  versus normalized crack length  $a/w$  for (001)-oriented Si. Black squares denote individual data points, red stars the experimental median of each  $a/w$  ratio. No significant difference was found between the two groups using a Mann-Whitney test.**

**Front view****Cut A-A**

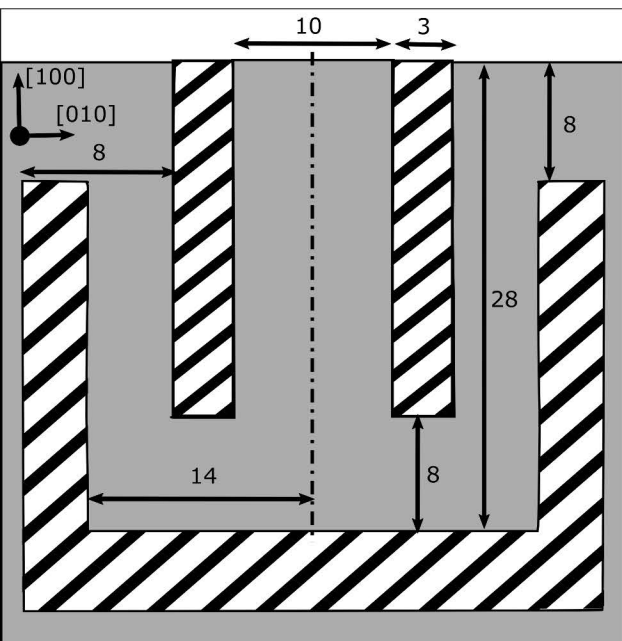




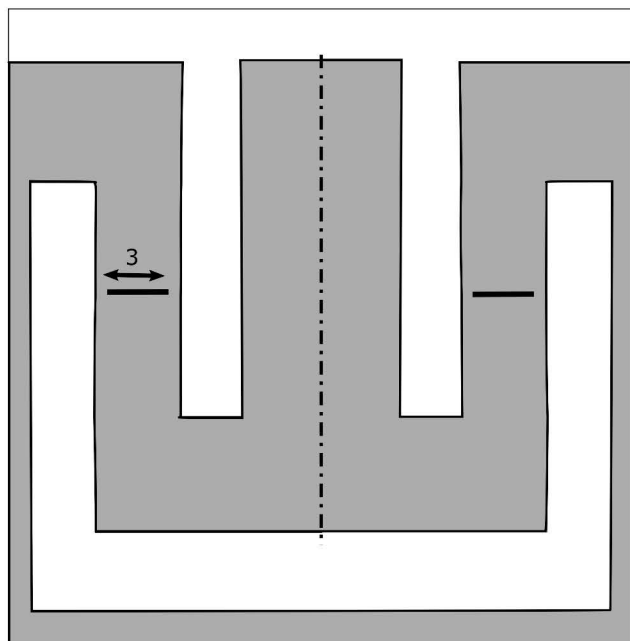




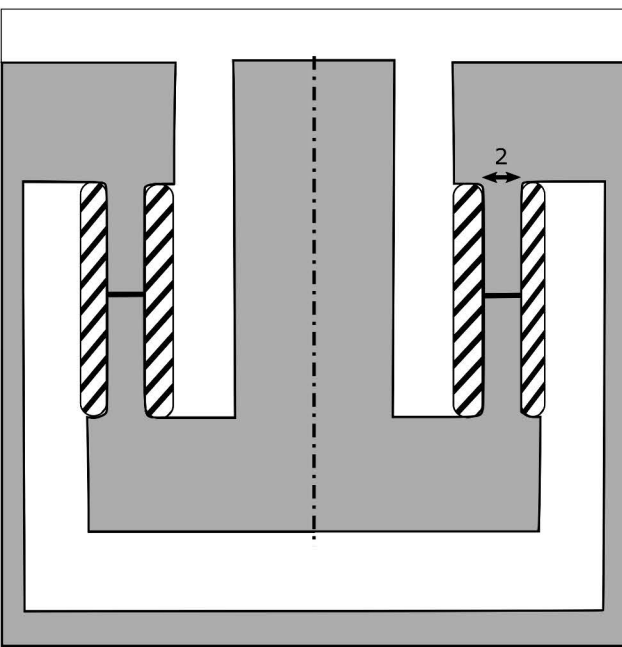
Rough cut (30kV)



Notch cut (15kV)



Fine polish (30kV)



Final sample

